Drying in porous media with gravity-stabilized fronts: Experimental results

A. G. Yiotis,[1] D. Salin,[1] E. S. Tajer,[2] and Y. C. Yortsos[2]

[1]*Laboratoire FAST, Universite Pierre & Marie Curie, Universite Paris-Sud, CNRS, Orsay 91405, France*

[2]*Mork Family Department of Chemical Engineering and Materials Science, University of Southern California, Los Angeles, California 90089-1450, USA*

In a recent paper [Yiotis *et al*., Phys. Rev. E **85**, 046308 (2012)] we developed a model for the drying of porous media in the presence of gravity. It incorporated effects of corner film flow, internal and external mass transfer, and the effect of gravity. Analytical results were derived when gravity opposes drying and hence leads to a stable percolation drying front. In this paper, we test the theory using laboratory experiments. A series of isothermal drying experiments in glass bead packings saturated with volatile hydrocarbons is conducted. The transparent glass cells containing the packing allow for the visual monitoring of the phase distribution patterns below the surface, including the formation of liquid films, as the gaseous phase invades the pore space, and for the control of the thickness of the diffusive mass boundary layer over the packing. The experimental results agree very well with theory, provided that the latter is generalized to account for the effects of corner roundness in the film region (which was neglected in the theoretical part). We demonstrate the existence of an early constant rate period (CRP), which lasts as long as the films saturate the surface of the packing, and of a subsequent falling rate period (FRP), which begins practically after the detachment of the film tips from the external surface. During the CRP, the process is controlled by diffusion within the stagnant gaseous phase in the upper part of the cells, yielding a Stefan tube problem solution. During the FRP, the process is controlled by diffusion within the packing, with a drying rate inversely proportional to the observed position of the film tips in the cell. Theoretical and experimental results compare favorably for a specific value of the roundness of the films, which is found to be constant and equal to 0.2 for various conditions, and verify the theoretical dependence on the capillary Ca_f, Bond Bo, and Sherwood Sh numbers.

I. INTRODUCTION

Fluid flow through liquid films that form at the pore walls, as the bulk liquid-gas menisci recede in the pore space, is an important transport mechanism in the drying of porous media [1–3]. Resembling corner flow in a capillary tube of polygonal cross section [4,5], flow in the films is driven by capillarity-induced pressure gradients (capillary wicking action) due to changes in the radius of curvature of the liquid-gas meniscus along the films. This action provides hydraulic connectivity between bulk liquid regions that appear macroscopically isolated and at the early stages of drying helps maintaining the surface of the porous material partially saturated, as the films reach all the way from the percolation front to the surface. This mechanism enhances drying rates and results in faster recovery times [6–8].

As the bulk liquid-gas meninsci (percolation front) recede in the pore space, the surface wetness (saturation) decreases because viscous effects and gravity in the films gradually take control over capillarity [6,9]. However, as long as liquid films still reach the external surface, the partial pressure of the evaporating species there remains practically constant and equal to the vapor pressure of the liquid (provided that the thickness of the external mass-transfer layer is significantly larger than the characteristic pore size of the medium [10], which is almost always the case). During this period, the process is controlled by external mass transfer and characterized by a constant recovery (drying) rate period (CRP), which depending on the type of drying the porous medium may last up to significant times [8,11–13].

At a critical film length x_p^c, that for the case of a finite size medium corresponds also to a critical liquid saturation S_c, capillarity cannot sustain viscous flow anymore and the films detach from the external surface of the medium [6,9]. As the film tips further recede, a completely dry region of pores develops below the surface of the medium (Fig. 1). During this period, drying is controlled by mass transfer (typically by diffusion) through this increasingly larger dry region and the process is characterized by a falling recovery rate (FRP).

Theoretical studies of such drying processes have been based on models such as a pore-network representation of the porous medium (originally developed by Fatt [14]). From simple percolation [15,16], to models that include corner film flow [17,18], and more recently, the effect of an external mass-transfer boundary layer [11], these models have included increasingly more complex phenomena. In our companion paper [19], we concentrated on the effects of gravity and viscosity that can play an important role on the extent of the film region [20,21]. Assuming perfectly sharp corners in the capillary cross sections, we derived analytical results when gravity opposes drying, hence leading to stabilized patterns, for key variables including drying rates, the transition between the constant (CRP) and falling rate (FRP) periods, and the extent of the film region. We were thus able to quantify the effect of parameters, such as a film-based capillary number Ca_f, that expresses the ratio of viscous forces in the films due to evaporation over capillary forces, the Bond number Bo, expressing the ratio of gravity to capillarity, and a Sherwood number Sh for external mass transfer.
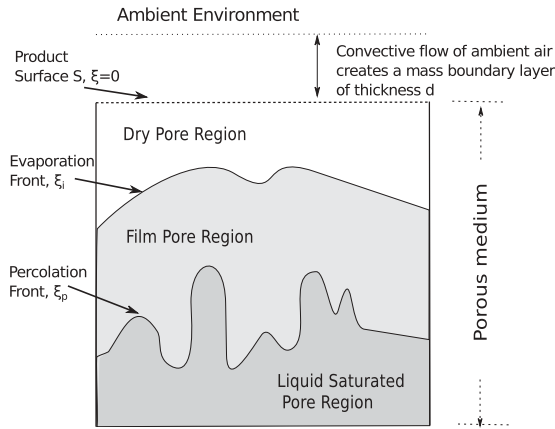
FIG. 1. Schematic of the characteristic pore regions that develop during the drying of porous media. During the falling rate period, three regions of pores can be identified: a far-field, liquid-saturated region, an intermediate region where vapor occupies the core of the pores but the pore walls remain covered by liquid films, and a completely dry region of pores just below the surface of the medium (from Yiotis *et al.* [9]).

In this paper, we present experimental results in geometries and under conditions that mimic the theoretical ones, with the specific objective to compare analytical and experimental results, and test the validity of the theoretical model. A nontrivial modification is implemented in the theory to account for the effects of corner roundness [4,5,21], which is expected to play a significant role in the present geometry, which involves a packing of spheres. We find excellent qualitative and quantitative agreement when the roundness coefficient takes a value of about 0.20, which appears remarkably constant for all configurations tested. As predicted in the theory, the CRP is related directly to the wicking action through the films that keep the surface of the medium partially saturated for long periods, resulting in a process controlled solely by external mass transfer; the onset of FRP is directly related to the films depinning from the product surface and the development of a completely dry region within the porous medium. Mass transfer by diffusion in this dry region controls the process during FRP, with the drying rates corresponding to a vapor-saturated interface at the observed position of the film tips.

II. EXPERIMENTAL PART

A. Experimental setup

We study the drying of glass bead packings, saturated with either *n*-pentane or *n*-hexane in the geometry of Fig. 2. The packings are placed in thin glass cells (akin to a Hele-Shaw cell) with the top side open to the ambient environment and are left to dry at environmental conditions. To avoid complications of external mass transfer, the external surface of the packings is deliberately below the top of the cell, creating a porous medium-free space (denoted as empty cell above). The thickness of this empty region δ is a parameter in our study. During drying, the weight of the cell and phase distribution patterns inside the packing are monitored with an analytical balance and a digital camera, both of which are computer
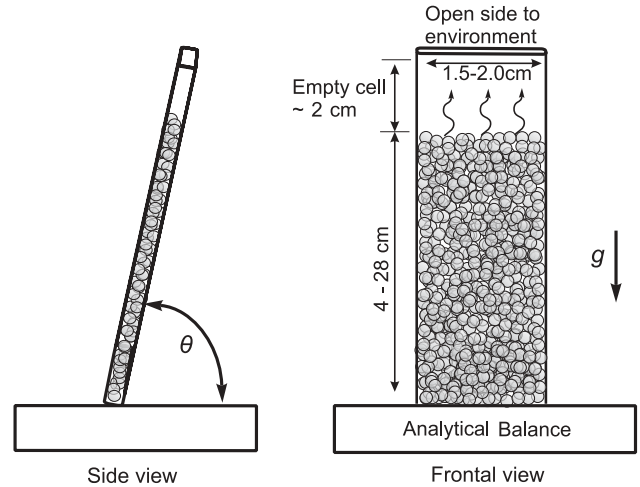

FIG. 2. Schematic of the experimental setup used in this study.

controlled. The physical properties of the evaporating fluids used in this study are shown in Table I.

The cells, used for the packings, were constructed from commercially available capillary cells (Vitrocom) of large aspect ratio (cross sections 15×1 and 20×2 mm^2) with rounded inner corners in order to minimize the formation of wetting liquid films at the sides of the cells, which would result in evaporation over the surface of the packing [21]. They were then cut at the desired length, with one side sealed with epoxy glue, while the other side was left open. Three different cells were constructed with lengths (heights) ranging from 60 to 300 mm (see Table II). A series of glass beads of different average sizes ranging from 100 to 850 μm with a known size distribution were used for the packings. The properties of the resulting porous media where determined by measuring the permeability and capillary rise in the packings placed in a 30-cm-long capillary tube connected to a Bernoulli tube. As a typical example, for a packing of 150–200 μm glass beads, we measured a porosity $\phi \simeq 40\%$, a permeability $\kappa = 1.3 \times 10^{-11}$ m^2, and a capillary rise $H = 0.17$ m for *n*-hexane. Perfectly wetting fluids were assumed, as expected for this particular porous medium.

The glass beads were initially mixed with the volatile liquid and left to rest for a few minutes before filling the cells. A packing protocol was followed in order to make the packing as dense and the surface of the packing as flat as possible. The cell was then positioned on an analytical mass balance (Sartorius CP225D with 0.01 mg accuracy) at an angle θ with respect to the horizontal surface and was exposed to drying at room temperature (ambient environment), which was controlled with an air-conditioning system. The temperature was recorded using a digital thermometer. During drying, the cell weight was recorded on a computer at 5–20 s intervals, depending on the experiment. In parallel, the movement of the drying front in the packing was monitored using a high-resolution digital camera (Nikon D300S), which was positioned in front and in parallel with the cell at the same angle θ with respect to the horizontal surface. The camera recorded snapshots of the phase distribution patterns in the cells at a resolution of 3216×2136 pixels^2 every 5–15 min. A halogen cold light source was positioned along the long side of the cell, in order

TABLE I. Physical properties used at 20°C–21°C, unless otherwise noted [22–25].

	n-Pentane	n-Hexane
Density ρ_l (kg m^{-3})	620	660
Viscosity μ (mPa s)	0.24	0.31
Surface tension γ (mN/m)	15.82	18.43
Binary diffusion coefficient D_{AB} in air (m^2/s)	8.6×10^{-6}	8.0×10^{-6}
Equilibrium vapor pressure P_e at 21°C (mmHg)	444.4	128.7
Equilibrium vapor pressure P_e at 24°C (mmHg)	497.8	147.0
Apparent diffusion coefficient D_M at 24°C (m^2/s)	13.2×10^{-6}	8.9×10^{-6}
Capillary length $L_c = \sqrt{\gamma/\rho_l g}$ at 24°C m	1.57×10^{-3}	1.69×10^{-3}

to enhance the contrast of the different pore regions. This lighting position was found to offer the best contrast between the film and completely dry regions, which are the focus of our study.

B. Typical experiments

A series of drying experiments was performed with packings of different bead sizes, cell angles, and cell filling heights to investigate the effect of gravity, capillarity, and evaporation conditions through the corresponding dimensionless numbers. The dynamics of the drying process and particularly the extent of the film region, which is believed to determine the transition between the constant recovery and the falling rate periods in drying, were a particular focus. Table II shows the experimental conditions for the different experiments. In all cases the average room temperature ranged between 19 °C

TABLE II. Parameters for the drying experiments. r_0 denotes the average bead radius, δ is the length of the upper empty part of the cell that serves as a mass boundary layer, T is the average room temperature during the experiments, θ is the cell inclination angle, and $\dot{J}_{CRP}$ is the measured drying rate during the CRP.

|	Number	r_0 [μm]	δ [mm]	θ [°]	T [°C]	$\dot{J}_{CRP}$ [g/s]
Cell 1	180211	150–200	16.58	90	21.5	4.52×10^{-6}
$15 \times 1 \times 56.6$ mm	250511	150–200	15.48	90	23.5	5.25×10^{-6}
hexane	170211	250–300	16.56	90	21.5	4.54×10^{-6}
	180511	250–300	15.89	90	22.5	4.92×10^{-6}
	100211	300–315	16.70	90	21.5	4.46×10^{-6}
	190511	300–315	15.84	90	23.0	5.04×10^{-6}
	140211	315–400	16.53	90	21.5	4.53×10^{-6}
	200511	315–400	15.72	90	23.5	5.17×10^{-6}
	150211	400–500	16.70	90	21.5	4.48×10^{-6}
	240511	400–500	16.95	90	23.5	4.80×10^{-6}
	080611	400–500	16.69	90	22.5	4.69×10^{-6}
	230211	800–850	16.60	90	21.0	4.41×10^{-6}
Cell 2	180411	300–315	19.41	90	20.1	0.95×10^{-5}
$20 \times 2 \times 79.8$ mm	200411	315–400	20.06	90	21.5	0.96×10^{-5}
hexane	070411	400–500	19.37	90	20.1	1.09×10^{-5}
	090511	400–500	18.88	55	23.0	1.12×10^{-5}
	110511	400–500	18.41	31.5	23.5	1.18×10^{-5}
	150911	500–600	19.60	90	22.5	1.06×10^{-5}
	270911	500–600	18.52	31.5	21.5	1.07×10^{-5}
	220411	630–800	19.70	90	22.5	1.05×10^{-5}
	020511	630–800	20.60	65	20.5	0.93×10^{-5}
	160511	630–800	18.66	32	21.0	1.05×10^{-5}
	260411	800–850	19.70	90	22.5	1.05×10^{-5}
	290411	800–850	19.65	65	21.0	1.01×10^{-5}
	050511	800–850	19.40	55	20.0	0.96×10^{-5}
	120511	800–850	19.10	31.5	23.0	1.11×10^{-5}
Cell 3	010312	100–160	17.30	90	23.5	5.52×10^{-5}
$20 \times 2 \times 300.0$ mm	220212	150–200	18.08	90	23.5	5.28×10^{-5}
pentane	270212	200–250	18.12	90	23.5	5.27×10^{-5}
	080212	300–315	19.00	90	22.8	4.86×10^{-5}
	010212	400–500	18.97	90	22.5	4.79×10^{-5}
	170212	500–600	18.79	90	23.5	5.08×10^{-5}
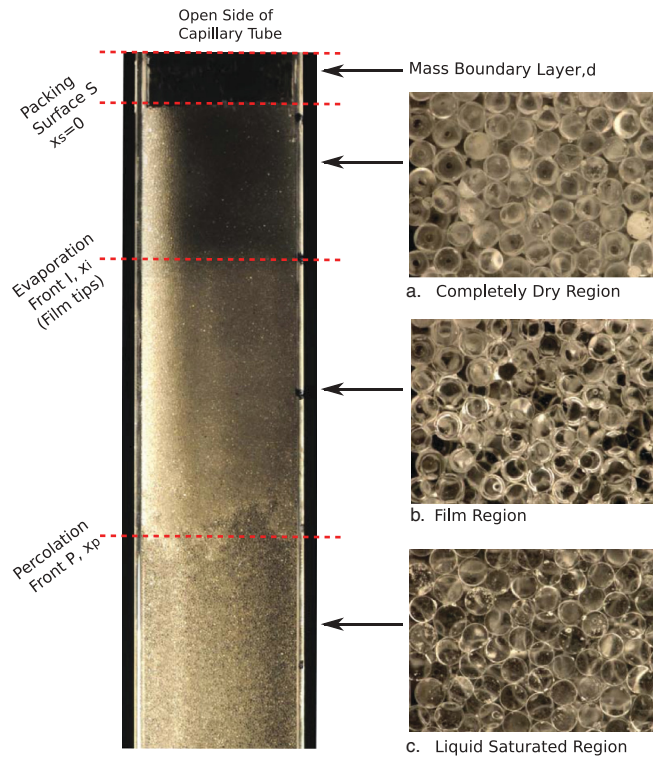
FIG. 3. (Color online) Typical phase distribution patterns observed during the drying experiments at a time when all regimes have developed. From top (open side of the tube) to bottom, we can distinguish the empty part of the cell that serves as external mass transfer, a completely dry region, a region where the beads are covered by liquid films (film region), and a liquid-saturated region. Pictures on the right are high-magnification images obtained by digital microscopy.

and 24 °C. Under these conditions, a typical experiment with n-hexane required approximately 30 hours up to 10 days for completion, depending on the cell size.

The recording of drying offers significant insight into the dynamics of the process and reveals the distinct regions in the packings where different mass-transport mechanisms are expected to be dominant [26,27]. Figure 3 presents a typical camera snapshot at a later time, when all regimes have developed, and the corresponding high-magnification images of the regions obtained using a digital microscope (Keyence VHX-1000E with VH-Z20R zoom lens 20–200x). From top to bottom we can clearly distinguish an empty zone in the upper part of the cell (over the surface of the packing), where mass transfer occurs by diffusion. Following is a region with completely dry glass beads (denoted as dry region). Next, we distinguish a brighter region where the gas phase has invaded the cental part of the pores, while a continuous liquid film covers the beads (denoted as the film region). Lastly, there exists a darker-color, far-field region of beads corresponding to the fully-liquid-saturated region. Following the notation used in our companion paper [19], the dry and film regions are separated by the evaporation front (I), while the film and liquid-saturated regions are separated by the percolation front (P).

At the beginning of the experiment, the liquid-gas interfaces reside at the external surface of the packing, which is fully saturated with liquid. Any excess of liquid outside the porous medium is due to the method selected for filling the cells and it is not accounted for in the drying curves presented below. After any excess liquid evaporates, the liquid-gas interfaces recede into the packing, their movement controlled by the combined action of capillary, viscous, and gravity forces. The movement of this percolation front is typically governed by invasion percolation in a gradient of hydrostatic pressure [28] and, within the front region, bears the geometrical characteristics of a fractal object. The dimensionless width of the percolation front σ_p is known to scale with the Bond number as $\sigma_p \sim \text{Bo}^{-0.47}$, leading to a flatter front in the limit of a gravity-dominated process, namely, as Bo takes larger values. Given that the exponent involved in the scaling is close to $1/2$, it is worth noting that the dimensional width of the percolation front Σ can then be approximated to be in the order of $\Sigma/r_o \simeq 4\text{Bo}^{-1/2} \simeq 4L_c/r_0$ [28], and hence $\Sigma \simeq 4L_c \sim$ 6–8 mm, where $L_c = \sqrt{\gamma/(\rho_l g)}$ is the capillary length and r_0 the average bead size. The prediction that Σ is independent of the bead size was also observed in our experiments (see also Fig. 9 below).

Recorded snapshots, such as the one of Fig. 3, reveal that at early times the films span all the way from the percolation front to the upper surface of the packing, keeping it saturated with liquid. Video recordings, focusing at the film area just below the surface of the packing during this period, demonstrate that the film thickness fluctuates locally as the percolation front recedes in the pore space in a series of Haines jumps [29]. This effect supports the argument that the film region is practically continuous and hydraulically coupled with the percolation front and the underlying liquid-saturated region. Thus the film thickness fluctuates in response to the capillary pressure buildup in the bulk liquid phase, due to capillary pinning, and the subsequent pressure relaxation when pores are invaded, as the capillary entry pressure is exceeded.

As the percolation front recedes deeper in the packing, the films eventually detach from the product surface and a completely dry region develops in the upper part of the packing [29]. High-magnification images taken from this region confirm that the beads are indeed completely dry (Fig. 3). According to the theory presented in our companion paper, the interface between the beads covered with films and the completely dry region (the evaporation front) marks the position where liquid evaporation takes place within the packing. This assumption will be tested later in this study. The evaporation front appears to be flat and recedes quite smoothly in the medium (as opposed to the movement of the percolation front, which occurs in jumps as described above). The average position of the evaporation front, denoted as $x_i \leqslant 0$, decreases with time following the movement of the percolation front [29]. Note that following the terminology of the first part [19], distances are marked from the product surface and are all negative (e.g., x_i, x_p, etc.).

In the following sections we will investigate the dynamics of both evaporation and percolation fronts, as well as the extent of the film region $x_i - x_p$, and compare theory and experiments.

III. COMPARISON BETWEEN THEORY AND EXPERIMENTS

A. Effect of rounded-corner films

In the theoretical part of this series [19], we defined the dimensionless film-based capillary Ca_f and Bond Bo numbers as follows:

$$Ca_f = \frac{\beta}{C^*} \frac{3\pi \mu D_M C_e}{\gamma \rho_l r_0}, \quad Bo = \frac{\rho_l r_0^2 g \sin\theta}{\gamma}, \quad (1)$$

where μ and ρ_l are the liquid viscosity and density, respectively, D_M is the apparent diffusion coefficient of the vapor through the gaseous phase, γ is the interfacial tension, C_e is the saturated vapor concentration, g the gravity acceleration, θ the angle of the cell plane with respect to the horizontal plane, and r_0 is the average bead radius. We recall that β and C^* denote, respectively, the dimensionless resistance to flow and the dimensionless film area. For a given polygonal cross section with sharp corners, these values are constant and independent of film thickness along the capillary and they were so taken in the theoretical part of this series. For example, values for these parameters under such conditions are available in the literature [4,5]. However, when the underlying geometry of the pore corners is not sharp (e.g., as shown in Fig. 4), these two parameters are no longer constant and in fact they vary with the film thickness. This means that the theory must be modified in two ways: First, by redefining the capillary number so that it remains a constant through the process, and second, by rederiving the expressions for the film thickness by taking into account the dependence of the film resistance to flow β and the cross-sectional area C^* on the local film thickness r.
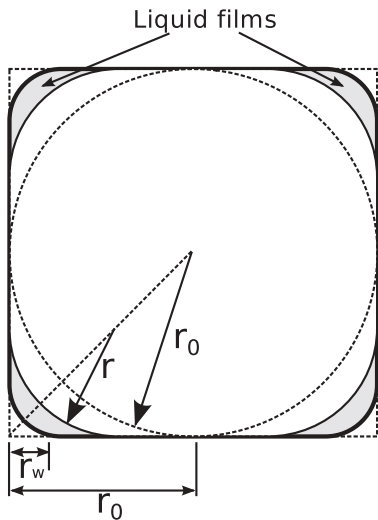

FIG. 4. Liquid films (gray area) of thickness r (or $\rho = r/r_0$ in dimensionless notation) in the cross section of a square capillary of size $2r_0$ with rounded corners. The film thickness varies from $\rho = 1$ (and $R_0 = p$) at the percolation front, where the films emanate (dashed circle), to $\rho = p$ (and $R_0 = 1$) at the film tips, where the films end (bold-faced line). Note that the roundness is $p = 0$ for a perfectly sharp corner and $p = 1$ for a cylindrical capillary.

To proceed, therefore, we define a modified capillary number (denoted by *),

$$Ca_f^* \equiv \frac{C^*}{\beta} Ca_f = \frac{3\pi \mu D_M C_e}{\gamma \rho_l r_0}, \quad (2)$$

which applies for all geometries, including polygonal cross sections. This capillary number expresses the ratio of viscous forces for flow driven by concentration gradients, to capillary forces, and typically takes a value of about 10^{-5}.

Then, we must express the variation of the parameters β and C^* with the film thickness. Consider the geometry in Fig. 4, where the corners of the capillary are rounded off. The roundness in this study is defined as $p = \frac{r_w}{r_0}$, which is independent of the local film thickness r. Note that $p = 0$ for a perfectly sharp corner (e.g., square capillary) and $p \to 1$ as $r_w \to r_0$ (cylindrical capillary). We obtain in a straightforward fashion, $C^* = (4 - \pi)[1 - (p/\rho)^2]$. However, the variation of β is more complex and requires significant calculations. Ransohoff and Radke [4] calculated β as a function of the so-called degree of roundness $R_0 = p/\rho$ (following the definition of Dong and Chatzis [5]), where $\rho = \frac{r}{r_0}$ is the dimensionless radius of the film. Note that, unlike p, the degree of roundness R_0 varies with the film thickness ρ, and thus it is not convenient for use in this study.

Figure 5 (left) shows the variation of β as a function of R_0, as well as a least-squares fit of the data calculated by Dong and Chatzis [5] for a square capillary. For our problem we must express these data as a function of the film thickness for a fixed value of p. The results are shown in Fig. 5 (right). One notes the significant variation of the dimensionless flow resistance β along the film, as the radius changes from the film tips, where $\rho = p$, to the percolation front (where $\rho = 1$). (Note that because of the roundness, the films now terminate when $\rho = p$, in contrast to $\rho = 0$ for polygonal cross sections.) It is evident that the effect of the corner roundness becomes important as p takes values greater than zero. This dependence was ignored in the first part of this series [19], which assumed a perfectly sharp corner, namely, $p \to 0$. However, it will be implemented in the following sections in order to compare theory and experiments.

B. Drying curves

A macroscopic measure of drying is the drying curve, expressing recovery rates as a function of time t or the remaining overall liquid fraction (saturation) S. The drying curves were obtained from the weight measurements of the cells recorded by the analytical balance and compared to the completely dry cell at the end of each experiment. As was also noted above, the early time measurements corresponding to an excess of liquid over the surface of the packing were subtracted and not accounted for. A moving average smoothing algorithm was applied to the recorded data to suppress higher frequency fluctuations in the recorded cell weight. These fluctuations are due to environmental parameters, such as room temperature variations. A 5–30 min averaging is applied, depending on the size of the cell.

A typical drying curve, showing the normalized drying rate e versus time, is presented in the logarithmic plot of Fig. 6. As expected, the curve exhibits two characteristic periods: (i)
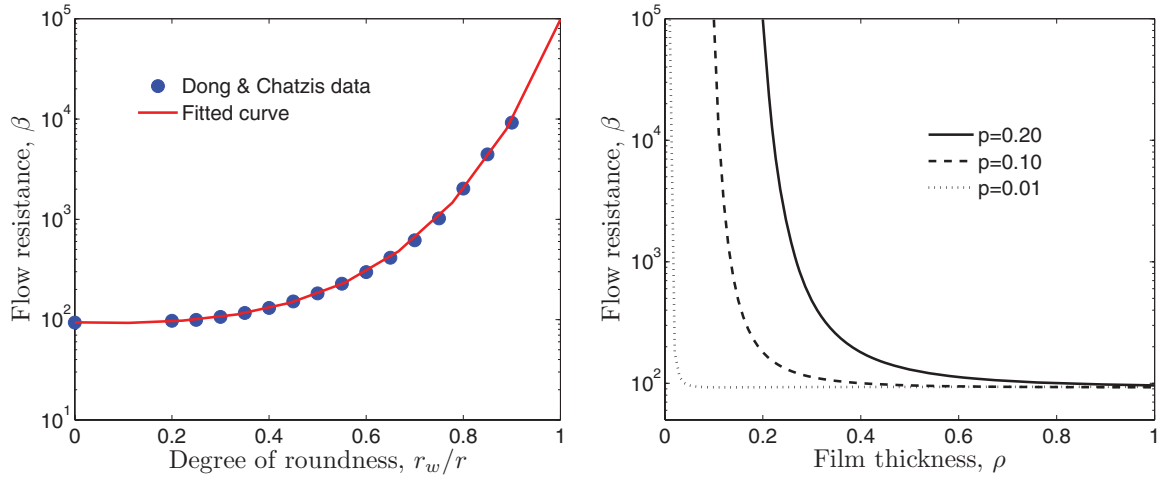
FIG. 5. (Color online) (Left) Dimensionless flow resistance β vs the degree of corner roundness $R_0 = r_w/r$, where r and r_w are the radii of curvature of the film and the corner, respectively (data adapted from Dong and Chatzis [5]). The continuous curve shows the least-squares fit used to calculate β. (Right) Dimensionless flow resistance β vs the film thickness $\rho = r/r_0$ along the capillary for different values of $p = r_w/r_0$. Note the divergence of the flow resistance as $\rho \to p$.

An early stage period, commonly known as the constant rate period (CRP), where the recovery rate is practically constant. Depending on the size of the beads and the angle and size of the cell in our experiments, this period may account for a significant amount of the recovered liquid saturation (see also Fig. 12). (ii) A late-time recovery period, known as the falling rate period (FRP), where the recovery rate decreases continuously with time. This period lasts until the packing becomes completely dry. It is interesting to note the power law dependence of the drying rate with time during later times in the FRP, which tends to $1/\sqrt{t}$, as expected [3].
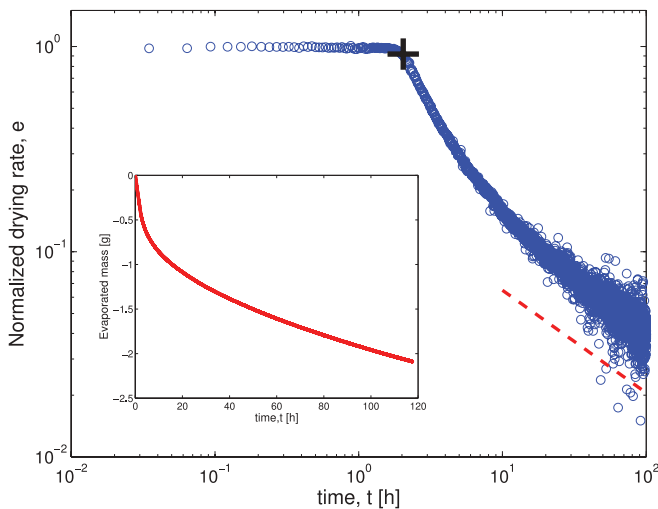

FIG. 6. (Color online) Experimental results for a typical drying curve in the 30-cm-long tube for a packing of 150–200 μm beads saturated with pentane. Drying rates are normalized with the Stefan tube solution in the upper (empty) part of the cell. The cross ($+$) marks the point when complete film detachment from the external surface is observed. The inset shows the corresponding dimensional variables. Shown with a dashed line is also the theoretical $1/\sqrt{t}$ dependence at later times.

Based on the recorded patterns, we can obtain insight on the dynamics of the CRP to FRP transition. In Fig. 6 we have plotted the point (cross mark) that corresponds to the liquid saturation when the film tips completely detach from the surface of the packing and a completely dry region begins to develop. This value, denoted as the critical saturation S_c in this study, coincides in all our experiments with the CRP to FRP transition in the drying curves. This result supports the argument raised in the theoretical part of this series, that the films keep the surface of the medium saturated even as the percolation front recedes deep in the pore space. Given that the parameters associated with external mass transport are fixed within the empty upper part of the cell, the above also implies that during the CRP all the liquid is provided from the percolation front towards the evaporation position through the wicking action of the liquid films.

1. Constant rate period

As also discussed above, during the CRP films reach all the way to the external surface of the porous medium, and drying is controlled by external diffusion across a layer of thickness δ. The resulting mass flux $\dot{\Im}_{CRP}$ can be modeled in our system by the classical Stefan tube solution for mass transport through a stagnant fluid [30],

$$\dot{\Im}_{CRP} = M \frac{P}{RT} \frac{D_M}{\delta}(y_S - y_\delta), \tag{3}$$

where y_S, y_δ are the mole fractions of the liquid vapors at the external surface of the packing and the open side of the tube, respectively, P and T are pressure and temperature, respectively, M is the molecular weight, and R the ideal gas constant. The apparent molecular diffusion coefficient in the upper part of the tube D_M is related to the molecular diffusivity D_{AB} as $D_M \simeq D_{AB}[1 + \frac{1}{2}(y_S + y_\delta) + \frac{1}{3}(y_S^2 + y_S y_\delta + y_\delta^2)]$ (see Table I). Note that for the case of hexane where $y_S < 0.2$, mass transport in the empty part of the cell can be simply described by Fickian diffusion with less than 10% error. In the case of pentane, however, the higher-order terms in

the above equation are required. A careful inspection of the measured CRP recovery rates reveals that they are always in good agreement with the rates predicted by Eq. (3) subject to boundary conditions $y_S = \frac{P^o}{P}$ and $y_\delta = 0$, where P^o is the vapor pressure of the liquid species. Namely, the vapor concentration of the liquid is found equal to zero at the tip of the drying cell. Therefore, in all results presented herein, we have used the normalized recovery rates, $e = \frac{\dot{\Im}}{\dot{\Im}_{CRP}}$.

2. Falling rate period

As discussed above, in all experiments the transition from CRP to FRP was found to coincide with the film tips detaching from the external surface and the development of a completely dry region of beads in the upper part of the packing. In the theoretical part we proposed that evaporation takes place primarily at the film tips (the evaporation front). Based on this assumption, the normalized drying rate can be expressed as a function of the average position of the evaporation front x_i below the surface:

$$e = \frac{\dot{\Im}}{\dot{\Im}_{CRP}} = \frac{1}{1 - \mathrm{Sh}\xi_i} = \frac{1}{1 - kx_i}, \qquad (4)$$

where Sh is the Sherwood number, defined in Part 1 as $\mathrm{Sh} = D_M/(D_{\mathrm{eff}}d)$, $\xi_i = x_i/r_0$, and $k = \mathrm{Sh}/r_0$. To test the validity of this expression, we plot in Fig. 7 the rescaled drying rate $\frac{1}{e} - 1$ versus the recorded position of the evaporation front x_i for a series of experiments with packings of different bead sizes ranging from 100 to 850 μm, but with a fixed thickness $\delta \simeq 0.19$ m of the external mass-transfer layer in the upper part of the tube. The observed linear dependence is in full agreement with the theory and supports the argument that evaporation occurs primarily at the film tips x_i. The slope $k = \mathrm{Sh}/r_0 = D_M/(D_{\mathrm{eff}}\delta)$ is found to be equal to $k = (160 \pm 10)$ m^{-1} and allows us to infer the effective diffusion coefficient in the
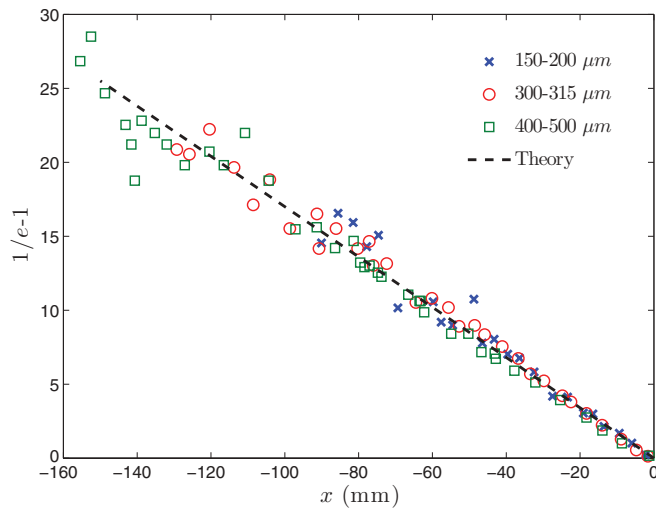

FIG. 7. (Color online) Rescaled evaporation rate $1/e - 1$ vs the recorded position of the film tips x_i for experiments with packings of different bead sizes. A linear dependence of the drying rate with the position of the film tips x_i is evident, supporting the argument that the evaporation front coincides with the observed position of the film tips. The slope of the fitted dashed curve is equal to $D_M/D_{\mathrm{eff}}/\delta$, independent of pore size. Note that δ is constant in these experiments.

porous medium as $D_M/D_{\mathrm{eff}} = F = k\delta$, where F is the so-called formation factor [31]. We find that $D_{\mathrm{eff}}/D_M \simeq 0.33$ is in good agreement with the expected value for a packing of spherical beads of porosity $\phi = 0.4$, typically deduced by expressions such as [31–33]

$$D_{\mathrm{eff}}/D_M = 1 - 3(1 - \phi)/2 + 3(0.89)(1 - \phi)^2/4. \qquad (5)$$

The above results support the argument that evaporation takes place primarily at the observed position of the film tips x_i, and the overlying region of beads is completely dry.

C. Effects of capillarity, gravity, and viscosity

We proceed with the analysis of the experimental results by considering the relationship between the location of the percolation front x_p and that of the evaporation front x_i, which determines both the critical extent of the film region x_p^c, when the films detach from the surface of the packing, and the evolution of the film extent during the FRP. This relationship depends strongly on Ca$_f$, Bo, and Sh, and for the simpler case when the geometrical parameters β and C^* remain constant along the film, i.e., when the corners are perfectly sharp, the following was found [19]:

$$x_i - x_p = \frac{1 - kx_i}{k\mathrm{Ca}_f}\,_2F_1\left[1, 3/4, 7/4, -3\mathrm{Bo}\frac{(1 - kx_i)}{kr_0\mathrm{Ca}_f}\right], \qquad (6)$$

where $_2F_1[a, b, c, z]$ is a hypergeometric function. In the more general case, however, and indeed in this experimental work, where the pore space of spherical beads is expected to include rounded corners, Ca$_f$ is no longer constant and the analytical solution must be modified.

We proceed in similar fashion as in the theoretical part of this series [19], but we now consider the dependence of β and C^* on the film thickness ρ and introduce Ca$_f^*$, as noted above. We use a least-squares fit on the data of Dong and Chatzis [5], as shown in Fig. 5 (left), and likewise use $C^* = (4 - \pi)[1 - (p/\rho)^2]$. We can then determine the extent of the film region from the solution of the integral equation

$$\int_{\rho=p}^{1} \frac{3\rho^2 d\rho}{\frac{\mathrm{Ca}_f^* \beta \mathrm{Sh}}{C^*(1 - \mathrm{Sh}\xi_i)} + 3\mathrm{Bo}\rho^4} = \xi_i - \xi_p, \qquad (7)$$

where all lengths have been normalized with the capillary size r_0, namely, $\xi = x/r_0$. From the above discussion, the only adjustable parameter in the above equation is the corner roundness $p = r_w/r_0$.

For illustration, the effect of the corner roundness on the extent of the film region is shown in Fig. 8 for different values of p. The critical film extent, when the film tips detach from the product surface, is also marked with circles joined with a dot-dashed line. In the absence of roundness, where $p = 0$, the solution is given by Eq. (6). Corner roundness has a significant effect on the extent of the film region, leading to shorter films for higher values of p. This is due to increased flow resistance as the film cross section becomes more round.

It is also interesting that the film extent increases as the percolation front recedes in the pore space, or equivalently, as the capillarity-induced pressure gradients in the films become smoother due to the progressively increased resistance to mass transport in the developing dry region. However, this
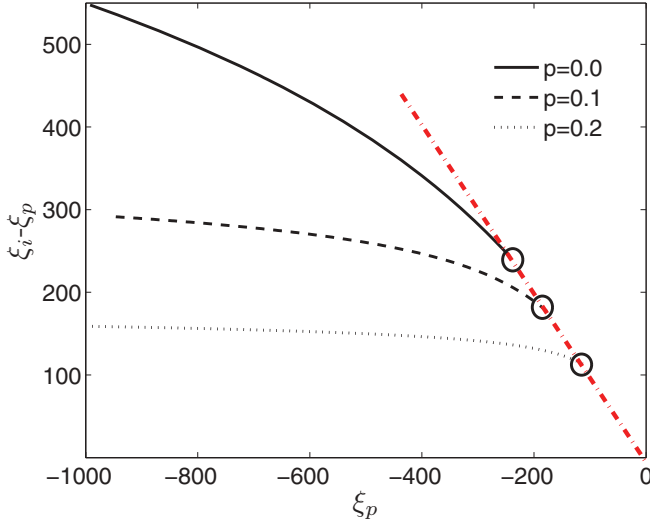
FIG. 8. (Color online) Effect of the corner roundness parameter p on the dimensionless extent of the film region $\xi_i - \xi_p$ for Bo = 1.95×10^{-2} and $Ca_f^* = 2.46 \times 10^{-5}$. Critical film extent is marked with circles (○) on the dot-dashed line. The solution for $p = 0$ corresponds to the analytical solution of Eq. (6), valid for sharp corners [19].

effect becomes negligible for higher values of the corner roundness, as also films become shorter. It useful to note that the corner roundness is a geometrical characteristic related to the roughness of the pore walls but independent of the pore size. Namely, porous media with rough pore walls, such as soils and other naturally occurring media, are expected to have values of $p \to 0$, and thus demonstrate nontrivial film flow effects (i.e., strong dependence of the film extent with the position of the percolation front and the evaporative demand through the Sherwood number).

The effect of the dimensionless parameters on the average film extent, as described by Eqs. (6) and (7), also suggests that higher values of Ca_f^*, Bo, and Sh lead to shorter films. Moreover, the extent of the film region increases as interfaces recede in the pore space and the drying rates decrease. These effects were also observed in our experiments. Images from the experiments demonstrating the determination of the location of both the evaporation x_i and percolation x_p fronts are shown in Fig. 9 for packings of different bead sizes. The snapshots are taken for the same position of the evaporation front x_i and fixed δ, and thus the same normalized drying rate e. Note that as the average bead size changes, it affects both the Bond number and the capillary number (through their dependence shown in Eqs. (1) and (2), respectively). The Bond number, being proportional to r_0^2, increases with the bead size, leading to increased gravity effects and shorter films. The capillary number is proportional to $1/r_0$, thus leading to stronger capillary forces and longer films. The extent of the film region in the snapshots of Fig. 9 is the result of these competing forces. In the limit of gravity-dominated processes, namely, sufficiently large values of Bo such those in Fig. 9, the extent of the film region decreases with increasing bead size.

Experimental results for the evolution of the film extent with x_p in the 30-cm cells and the bead sizes of Table III are shown in Fig. 10. The calculated values of the Bond number
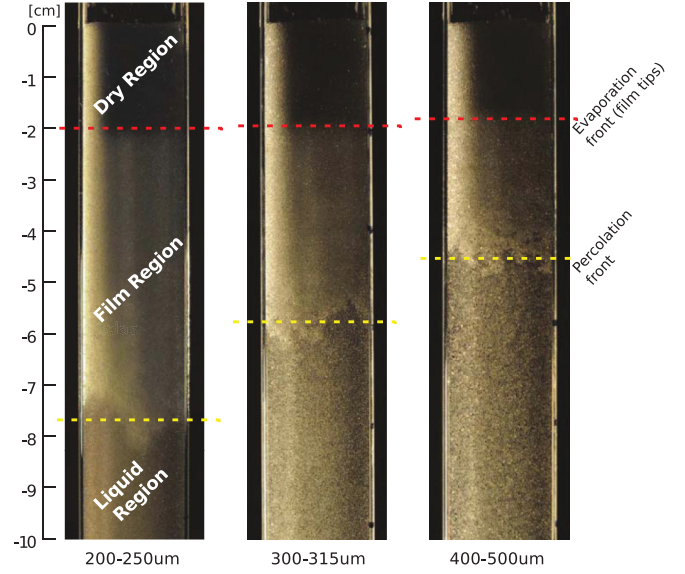

FIG. 9. (Color online) The location of evaporation and percolation fronts in experiments with different bead sizes, from left to right, 200–250 μm, 300–315 μm, and 400–500 μm. The snapshots are taken for the same position of the evaporation front x_i and thus the same normalized drying rate e. Note that the extent of the film region $x_i - x_p$ increases as x_p recedes.

indicate significant effects of gravity but rather weak effects of viscous forces (other than in the film region). The results were matched by comparing with the solution of Eq. (7) and using the adjustable parameter p. It is rather remarkable that excellent agreement is achieved for the same constant value of the roundness equal to $p = 0.19 \pm 0.02$ in all experiments, regardless of bead size, cell filling and inclination, and volatile liquid. We believe that this reflects the apparent self-similarity in the packings, independent of the scale defined by the bead size r_0.

A final comparison will be provided regarding the drying rate e vs liquid saturation curves. The overall liquid saturation S is defined as

$$S = \frac{S_b + S_f}{S_t}, \qquad (8)$$

where S_b, S_f, and S_t are the bulk liquid volume (between the percolation front and the bottom of the packing), the liquid volume contained in the films, and the initial total liquid saturations, respectively. Using geometric considerations, we find $S_b = (\xi_p - \xi_b)[4 - p^2(4 - \pi)]$ and $S_t = -\xi_b[4 - p^2(4 - \pi)]$

TABLE III. Calculated and fitted parameters (indicated by boldface) for the experimental data of Fig. 10.

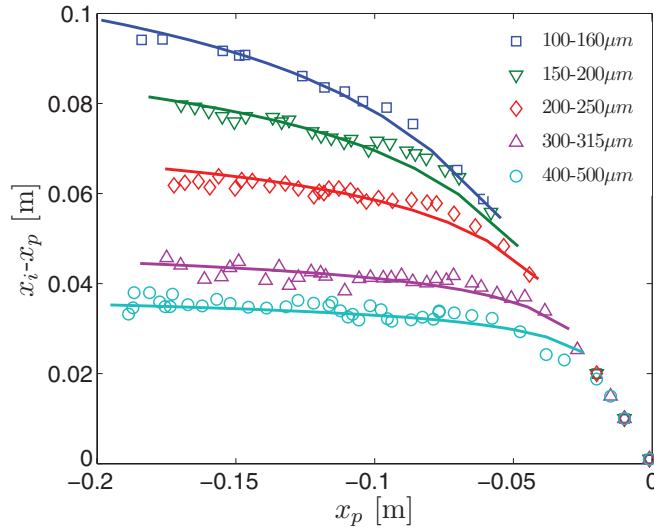|	r_0 [m]	Bo	Ca_f^*	p
100–160 μm	65.0×10^{-6}	1.62×10^{-3}	8.52×10^{-5}	**0.18**
150–200 μm	87.5×10^{-6}	2.94×10^{-3}	6.33×10^{-5}	**0.17**
200–250 μm	112.5×10^{-6}	4.87×10^{-3}	4.92×10^{-5}	**0.18**
300–315 μm	153.75×10^{-6}	9.09×10^{-3}	3.60×10^{-5}	**0.21**
400–500 μm	225.0×10^{-6}	19.50×10^{-3}	2.46×10^{-5}	**0.20**

FIG. 10. (Color online) Experimental results for the extent of the film region $x_i - x_p$ vs the position of the percolation front x_p for packings of different bead sizes. The film extent increases as the front recedes. The theoretical curves (continuous line) are obtained from the solution of Eq. (7) with a roundness parameter of approximately 0.2 for all curves, as shown in Table III. The dashed line marks the critical film extent when the films detach from the product surface.

and

$$S_f = (4 - \pi) \int_{\xi_i}^{\xi_p} (\rho^2 - p^2) d(-\xi)$$
$$= (4 - \pi) \left(\int_{\rho=p}^{1} \frac{3\rho^4 d\rho}{\mathrm{Ca}_f^* \frac{\beta}{C^*} \frac{\mathrm{Sh}}{1-\mathrm{Sh}\xi_i} + 3\mathrm{Bo}\rho^4} + (\xi_p - \xi_i)p^2 \right),$$
(9)

where ξ_b is the dimensionless length of the packing. In the above, the relationship between ξ_p and ξ_i is determined using Eq. (7). We can thus construct the full drying curve, $e = e(\xi_i)$ vs S.

Figure 11 shows experimental results for two packings of beads with sizes ranging between 100–160 μm and 400–500 μm in the longer 30-cm cell. In these experiments, gravity dominates, leading to earlier film detachment and shorter films, particularly for larger bead packings. The theoretical curves [from the solution of Eqs. (7), (8), and (9)] are also plotted using the fitted value of roundness p, as shown in Table III. Experimental and theoretical results are in very good agreement, except that film detachment in the experiments is gradual and the transition from CRP to FRP not as sharp as predicted by the one-dimensional model. This smooth transition can be modeled using a three-dimensional pore network model that captures the gradual depinning of the film tips forming the surface of the porous medium, and the corresponding decrease of the surface liquid saturation provided by the films [11].

Finally, we present results of the effect of gravity. Figure 12 shows drying curves for packings of the same bead size for different inclination angles θ and thus different values of the Bond number, while keeping Ca_f^* and Sh constant. Smaller inclination, and thus smaller Bo, lead to longer film regions
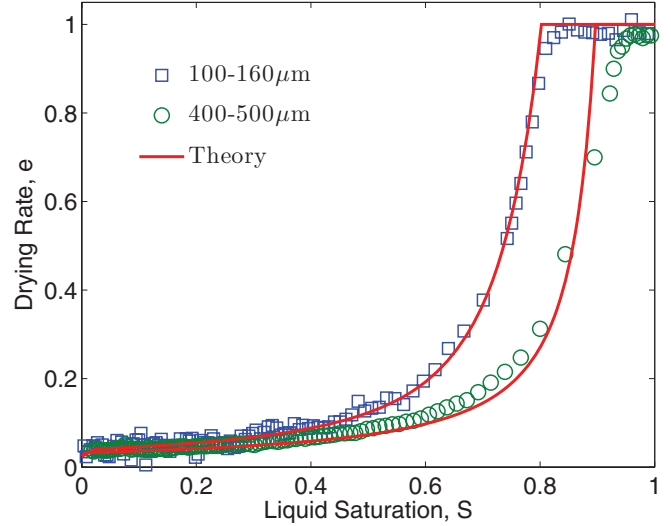

FIG. 11. (Color online) Experimental and predicted drying curves (continuous line) for two different bead packings of size 100–200 μm ($\square$) and 400–500 μm ($\bigcirc$) in the 30-cm cell saturated with pentane. The theoretical curves are obtained using the geometrical parameters of Table III.

(a result which is also visually confirmed) and a longer CRP. A clear dependence of the critical saturation S_c on the Bond number Bo is also evident. The comparison with the theory is quite good, although progressively deteriorating as the liquid saturation becomes very small. This is probably the result of additional complexity that cannot be captured adequately after the percolation front reaches the end of the cell (denoted by circles in Fig. 12).
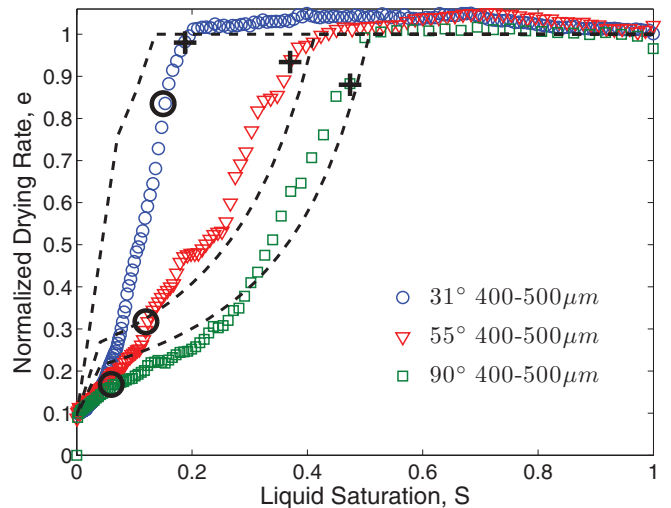

FIG. 12. (Color online) Experimental and theoretical drying curves at different inclinations θ of cell 2. Bead packings of size 400–500 μm saturated with n-hexane. Crosses ($+$) mark the observed saturation when the films detach completely from the external surface, while circles (o) mark the saturation when the bulk liquid region evaporates completely (the percolation front reaches the bottom of the cell). Dashed lines are the theoretical predictions for $p = 0.2$, $\mathrm{Ca}_f^* = 6.35 \times 10^{-6}$, and Bo $= 9.16 \times 10^{-3}$ for $\theta = 31°$, Bo $= 1.46 \times 10^{-2}$ for $\theta = 55°$, and Bo $= 1.78 \times 10^{-3}$ for $\theta = 90°$.

IV. CONCLUSIONS

We performed a series of isothermal drying experiments of glass bead packings, placed in transparent glass cells, initially saturated with volatile hydrocarbons. Our experimental setup allowed for the monitoring of the phase distribution patterns below the surface of the packing and the recording of the corresponding drying curves. We have been able to record the formation of macroscopic films at the surface of the glass beads and determine precisely the detachment time, as well as the film extent with respect to the position of the percolation front in the medium. Our results show that the drying curves exhibit two clear regimes: a constant rate period (CRP) that lasts practically as long as the films saturate the surface of the packing, and a falling rate period (FRP) that begins after the detachment of the film tips from the porous medium surface. Experimental evidence shows that during the CRP the process is controlled by mass transfer within the empty, upper part of the cell, yielding a solution identical to a Stefan tube problem. During the FRP, the process is controlled by diffusion within the packing, with a drying rate inversely proportional to the observed position of the film tips in the cell. The extent of the film region is found to be a function of a film-based capillary number Ca_f, the Bond number Bo, and a Sherwood number Sh. It is also found to increase with the receding percolation front, as predicted in the theoretical part of this series. We develop a generalization of our theoretical model to account for the effect of corner roundness in our bead packings. The results for the measured extent of the film region and the drying curves are in very good agreement with the theoretical predictions in the entire range of parameter values in this study for a single value of the introduced roundness coefficient equal to 0.2.

[1] J. V. Brakel, Adv. Drying **1**, 217 (1995).

[2] J. Laurindo and M. Prat, Chem. Eng. Sci. **53**, 2257 (1998).

[3] T. M. Shaw, Phys. Rev. Lett. **59**, 1671 (1987).

[4] T. Ransohoff and C. Radke, J. Colloid Interface Sci. **121**, 392 (1988).

[5] M. Dong and I. Chatzis, J. Colloid Interface Sci. **172**, 278 (1995).

[6] P. Lehmann, S. Assouline, and D. Or, Phys. Rev. E **77**, 056309 (2008).

[7] N. Shokri, P. Lehmann, P. Vontobel, and D. Or, Water Resour. Res. **44**, W06418 (2008).

[8] P. Faure and P. Coussot, Phys. Rev. E **82**, 036303 (2010).

[9] A. G. Yiotis, A. G. Boudouvis, A. K. Stubos, I. N. Tsimpanogiannis, and Y. C. Yortsos, Phys. Rev. E **68**, 037303 (2003).

[10] M. Suzuki and S. Maeda, J. Chem. Eng. Jpn. **1**, 26 (1968).

[11] A. Yiotis, I. Tsimpanogiannis, A. Stubos, and Y. Yortsos, Water Resour. Res. **43**, W06403 (2007).

[12] N. Shokri, P. Lehmann, and D. Or, Water Resour. Res. **45**, W06403 (2009).

[13] N. Shokri and D. Or, Water Resour. Res. **47**, W09513 (2011).

[14] I. Fatt, Trans. Am. Inst. Min., Metall. Pet. Eng. **207**, 144 (1956).

[15] M. Prat, Int. J. Multiphase Flow **19**, 691 (1993).

[16] M. Prat, Int. J. Multiphase Flow **21**, 875 (1995).

[17] A. G. Yiotis, A. G. Boudouvis, A. K. Stubos, I. N. Tsimpanogiannis, and Y. C. Yortsos, AIChE J. **50**, 2721 (2004).

[18] M. Prat, Int. J. Heat Mass Transfer **50**, 1455 (2007).

[19] A. G. Yiotis, D. Salin, E. S. Tajer, and Y. C. Yortsos, Phys. Rev. E **85**, 046308 (2012).

[20] F. Chauvet, P. Duru, S. Geoffroy, and M. Prat, Phys. Rev. Lett. **103**, 124502 (2009).

[21] F. Chauvet, P. Duru, and M. Prat, Phys. Fluids **22**, 112113 (2010).

[22] R. Reid and T. Sherwood, *The Properties of Gases and Liquids*, 2nd ed. (McGraw-Hill, New York, 1966).

[23] R. Weast and M. ASTLE, *CRC Handbook of Chemistry and Physics*, 63rd ed. (CRC Press, Boca Raton, FL, 1982).

[24] E. Cussler, *Diffusion: Mass Transfer in Fluid Systems*, 2nd ed. (Cambridge University Press, Cambridge, England, 1997).

[25] M. Nagasaka, J. Chem. Eng. Data **18**, 388 (1973).

[26] A. G. Yiotis, D. Salin, E. S. Tajer, and Y. C. Yortsos, http://www.fast.u-psud.fr/~yiotis/080212_300-315um_x4500.avi (2012).

[27] A. G. Yiotis, D. Salin, E. S. Tajer, and Y. C. Yortsos, http://www.fast.u-psud.fr/~yiotis/010212_400-500um_x4500.avi (2012).

[28] M. Chaouche, N. Rakotomalala, D. Salin, B. Xu, and Y. C. Yortsos, Phys. Rev. E **49**, 4133 (1994).

[29] A. G. Yiotis, D. Salin, E. S. Tajer, and Y. C. Yortsos, http://www.fast.u-psud.fr/~yiotis/190511_135203.avi (2012).

[30] R. Bird, W. Stewart, and E. Lightfoot, *Transport Phenomena*, 2nd ed. (John Wiley and Sons, New York, 2007).

[31] F. Dullien, *Porous Media: Fluid Transport and Pore Structure*, 2nd ed. (Academic Press, San Diego, 1992).

[32] A. Acrivos and E. Chang, Phys. Fluids **29**, 3 (1986).

[33] I.-S. Park, J. M. Smith, and B. J. McCoy, AIChE J. **33**, 1102 (1987).